ACS Catalysis
Research Article
pubs.acs.org/acscatalysis

Synthesis and Optical Properties of Ag(I), Pb(II), and Bi(III) Tantalate-Based Photocatalysts

Jonathan Boltersdorf, Tricia Wong, and Paul A. Maggard*

Department of Chemistry, North Carolina State University, Raleigh, North Carolina 27695-8204 United States

S Supporting Information

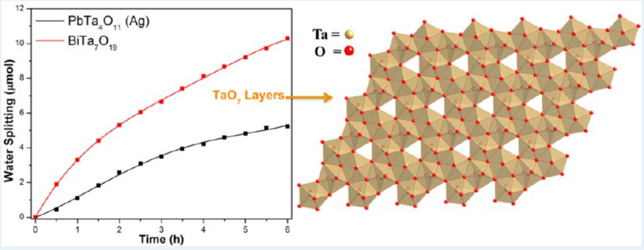

ABSTRACT: The Ag(I) and Bi(III) tantalates $Ag_2Ta_4O_{11}$, $BiTa_7O_{19}$, and $Bi_7Ta_3O_{18}$ were prepared by solid-state methods at 1000 °C for 24−48 h. The Pb(II)-containing tantalate $PbTa_2O_6$ was prepared at 1100 °C for 24 h, whereas $Pb_3Ta_4O_{13}$ and $PbTa_4O_{11}$ were synthesized from a reaction of $A_2Ta_4O_{11}$ (A = Na, Ag) precursors with a $PbCl_2$ flux (at 1:1, 5:1, and 10:1 molar ratios) at 700 °C from 24 to 96 h. The $PbTa_2O_6$, $Pb_3Ta_4O_{13}$, and $Bi_7Ta_3O_{18}$ structures consist of TaO_6 layers and TaO_6 chains/rings with Pb(II) ions located within the cavities. The structures of $Ag_2Ta_4O_{11}$, $PbTa_4O_{11}$, and $BiTa_7O_{19}$ consist of layers of TaO_7 pentagonal bipyramids that alternate with Ag(I), Pb(II), and Bi(III) cations, respectively. UV−vis diffuse reflectance data were used to measure bandgap sizes for $Ag_2Ta_4O_{11}$ (~3.9 eV), $PbTa_4O_{11}$ (~3.8−3.95 eV), $Pb_3Ta_4O_{13}$ (~3.0 eV), $PbTa_2O_6$ (~3.6 eV), $BiTa_7O_{19}$ (~3.6 eV), and $Bi_7Ta_3O_{18}$ (~2.75 eV). A decrease in the band gap was observed with an increase in the Pb(II) or Bi(III) content. Photocatalytic activities of the platinized samples in aqueous solutions under ultraviolet irradiation were found to range from ~7 to ~194 μmol $H_2 \cdot g^{-1} \cdot h^{-1}$ in aqueous methanol and from ~42 to ~213 μmol $O_2 \cdot g^{-1} \cdot h^{-1}$ in aqueous silver nitrate. Electronic-structure calculations based on density functional theory show the highest-energy valence band states consist of the respective Ag 4d orbital/Pb 6s orbital/Bi 6s orbital and O 2p orbital contributions, and the lowest-energy conduction band states arise from the Ta 5d orbital contributions. The latter are delocalized over the TaO_7 pentagonal bipyramid layers within the $A_2Ta_4O_{11}$ (A = Na, Ag), $PbTa_4O_{11}$, and $BiTa_7O_{19}$ structures. Nearly all of the tantalates exhibit significant water oxidation photocatalytic activity. However, higher activity for water reduction was found for tantalates consisting of TaO_7 pentagonal bipyramid layers that can serve as charge-migration pathways.

KEYWORDS: *photocatalysis, lead exchange, layered tantalate, solar energy, band engineering*

INTRODUCTION

Investigations of photocatalytic water splitting into H_2 and O_2 using solar energy have been of increasing importance owing to the global need for developing clean and renewable energy sources. Metal oxide photocatalysts are of particular interest for their ability to absorb solar photons that can be used to drive the water-splitting reactions at their surfaces. Requirements include that the energy of the incident photons must be greater than that of the band gap (E_g) of the metal oxide, with a conduction-band edge more negative than that of the proton reduction potential (−0.41 V vs NHE at pH = 7) and a valence band edge more positive than that of the water oxidation potential (+0.82 V vs NHE at pH = 7).[1−3] Thus, a bandgap size of ≥1.23 eV is required to drive water reduction and oxidation.[4] However, photocatalysts with small bandgap sizes that satisfy these conditions typically exhibit only short-lived stability under irradiation in solution (e.g., Cu_2O), whereas those with larger bandgap sizes are significantly more stable but absorb a smaller amount of solar energy (e.g., TiO_2, $NaTaO_3$).[3,5,6] Recent approaches for the discovery of novel metal oxide photocatalysts include doping by transition metals, varying their particle morphologies and sizes, nanoscaling effects, and the band engineering of metal oxides. One band engineering approach involves shifting the valence band energies via a flux-mediated exchange of cations within the structure. For example, the insertion of transition metals with filled d orbitals or s orbitals, such as Pb(II) and Bi(III) cations, can result in decreased bandgap sizes.[1−3,7−9] The filled s orbitals and d orbitals form a new higher-energy valence band, whereas the conduction band remains delocalized over empty d orbitals, such as for Ta(V) or Ti(IV).

Tantalates have been reported to be highly active photocatalysts for water reduction or oxidation. Alkali metal tantalates have exhibited some of the highest apparent quantum yields (~56% for $NaTaO_3$),[5,10,11] stability for more than 400 h under irradiation, and the capability of total water splitting without the aid of cocatalysts or sacrificial reagents.[1,2] Nearly all of these reported tantalate photocatalysts exhibit structures based on condensed TaO_6 octahedra layers or three-dimensional structures.[1,2,5,10] Recently, we have shown that the flux synthesis of natrotantite ($Na_2Ta_4O_{11}$)[12] yields a structurally new type of photocatalyst that consists of condensed TaO_7

Received: August 20, 2013
Revised: October 29, 2013
Published: October 30, 2013

dx.doi.org/10.1021/cs400707x | *ACS Catal.* 2013, 3, 2943−2953

pentagonal bipyramids.[13] Natrotantite is a member of the larger $A_xTa_{3n+1}O_{8n+3}$ (A = Na(I), Ag(I); $x = 1, 2$; $n = 1, 2$) family that can be modified by the incorporation of metal cations between the TaO_7 pentagonal bipyramid layers, for example, Ag(I), Pb(II), and Bi(III). Although many Pb- and Bi-based oxide photocatalysts have been reported, none so far have been investigated within this large family. Previously, Pb-containing oxides have been found to exhibit increased valence band energies owing to the O 2p and Pb 6s orbital interactions, resulting in smaller bandgap sizes.[9]

Reported herein are the solid state and flux-mediated syntheses of $Ag_2Ta_4O_{11}$, $PbTa_4O_{11}$, $PbTa_2O_6$, $Pb_3Ta_4O_{13}$, $BiTa_7O_{19}$, and $Bi_7Ta_3O_{18}$. Final products were characterized by powder X-ray diffraction (PXRD), UV−vis diffuse reflectance spectroscopy (DRS), X-ray photoelectron spectroscopy (XPS), and photocatalytic measurements of H_2 and O_2 production in aqueous solutions. Electronic structure calculations based on density functional theory were used to understand the influence of Pb(II) and Bi(III) cations on the bandgap sizes and photocatalytic activity of these tantalate phases.

■ METHOD

Synthesis. The solid-state syntheses of $Ag_2Ta_4O_{11}$, $BiTa_7O_{19}$, and $Bi_7Ta_3O_{18}$ were performed according to previously reported methods by combining stoichiometric mixtures of reagent grade Ag_2O (Alfa Aesar, 99.99%), Bi_2O_3 (Alfa Aesar, 99.99%), and Ta_2O_5 (Acros Organics, 99.99%). The reactants were ground in a mortar and pestle for 30 min, pressed into pellets, and heated within alumina crucibles inside a box furnace, then radiatively cooled to room temperature. $Ag_2Ta_4O_{11}$ was heated for 24 h at 1000 °C to yield a white powder, whereas $BiTa_7O_{19}$ and $Bi_7Ta_3O_{18}$ were heated for 48 h at 1000 °C to yield yellow powders.[14−17]

The flux synthesis of the layered natrotantite, $Na_2Ta_4O_{11}$,[12,13] was performed according to previously reported methods by grinding stoichiometric amounts of Na_2CO_3 (Alfa Aesar, 98%) and Ta_2O_5 in a mortar and pestle, which was then combined with a 50% K_2SO_4 (Fisher Scientific, 99.8%) and 50% Na_2SO_4 (Alpha Aesar, 99.0%) eutectic flux in a 12:1 flux-to-reactant molar ratio. The mixture was ground together and heated in an alumina crucible for 2 h at 1000 °C inside a box furnace, followed by a 30 min cool-down time. The excess K_2SO_4/Na_2SO_4 flux was removed by washing and centrifuging with deionized water, followed by drying in an oven at 80 °C for 12 h.[13] $PbTa_4O_{11}$ was prepared in an ion-exchange reaction by heating the as-prepared $A_2Ta_4O_{11}$ (A = Na, Ag) within a $PbCl_2$ (Alfa Aesar, 99.99%) flux in 1:1, 5:1, and 10:1 flux-to-reactant molar ratios. The reactants and flux were ground together in an evacuated and flame-sealed fused-silica tube that was heated for 96 h at 700 °C. The products were washed and centrifuged using a sequence of concentrated NH_4OH, deionized water, and concentrated HCl to remove excess ions, AgCl, and $PbCl_2$; this procedure yielded a fine gray powder.[18] The cubic pyrochlore-related $Pb_3Ta_4O_{13}$ was prepared using a similar high-temperature ion-exchange reaction of $Na_2Ta_4O_{11}$ with $PbCl_2$ (10:1 flux-to-reactant molar ratio) in air in an alumina crucible for 24 h at 700 °C with 1 h ramp-up and cool-down times. The products were washed and centrifuged using a dilute NH_4OH solution to yield pale yellow crystals. Synthesis of $Pb_3Ta_4O_{13}$ has previously been reported using only solid state methods, but not by flux-mediated ion-exchange methods.[19,20]

The solid state synthesis of the tungsten bronze, $PbTa_2O_6$, was performed by combining a stoichiometric mixture of reagent grade PbO (Alfa Aesar, 99.999%) and Ta_2O_5 in a 1:2 molar ratio, then grinding, pelletizing, and heating in an alumina crucible in air for 24 h at 1100 °C. The products were radiatively cooled to room temperature inside a box furnace to yield a white powder. An alternative procedure of this solid state synthesis has previously been reported by Ravez et al.[21,22]

Characterization. High-resolution powder X-ray diffraction (PXRD) data were collected on an INEL diffractometer using Cu $K\alpha_1$ ($\lambda = 1.54056$ Å) radiation from a sealed-tube X-ray source (35 kV, 30 mA) equipped with a curved position-sensitive detector (CPS120) as well as on a Rigaku R-Axis Spider with a curved image-plate detector. UV−vis diffuse reflectance spectra were collected on a Shimadzu UV-3600 equipped with an integrating sphere. A pressed barium sulfate disc was used as the background, and the data were transformed using the Kubelka−Munk, $F(R)$, function.[23] Tauc plots were plotted as $(F(R) \times h\nu)^n$ vs $h\nu$ (eV), where $n = 2$ for direct and $n = {}^1/_2$ for indirect band gap transitions. The bandgap size was then measured at the intersection of the baseline with the linear rise of the parabolic curve.[24] X-ray photoelectron spectroscopy measurements (Riber MAC2 XPS) were carried out in an ultrahigh vacuum chamber (base pressure 5×10^{-10} Torr) with a cylindrical mirror-type electron spectrometer at 54.7°. Nonmonochromatic Mg $K\alpha$ radiation (1253.6 eV) was used as the excitation source. Energy resolutions for survey and detail scans were ∼2 and ∼1 eV, respectively. Energy scales were calibrated by assigning adventitious 1s carbon peaks at 284.5 eV. Powder samples were placed on carbon tape (Ted Pella) on sample holders in ambient air and immediately loaded into the XPS chamber to be brought under vacuum. Spectra were analyzed using commercial CasaXPS software (version 2.3.16).[25] The Shirley method was used for background subtraction, and spectral lines for curve-fitting were fitted with 70% Gaussian and 30% Lorentzian asymmetric line shapes.[25−27]

Photocatalytic Measurements. Prior to phototesting, samples were loaded with a 1 wt % platinum cocatalyst using the photochemical deposition (PCD) method.[5,7,13] Approximately 150 mg of each sample was added to 30 mL of an aqueous dihydrogen hexachloroplatinate (IV) solution ($H_2PtCl_6 \cdot 6H_2O$; Alfa Aesar, 99.95%); which was then irradiated for ∼2−4 h in an outer-irradiation type fused-silica reaction cell using a 400 W Xe arc lamp under constant stirring with a magnetic stir bar. This photochemical deposition of platinum nanoislands on particle surfaces is used as a kinetic aid to increase the rate of electron transfer across the surface of the particle and to serve as a more rapid proton reduction site.[26−35] Methanol (∼2 mL) is added as a sacrificial reagent to increase the amount of platinum formation on the surfaces of the particles.[30] After irradiation, the samples were washed and centrifuged with deionized water to remove excess Cl^- ions and dried in an oven at 80 °C for 12 h.

The photocatalytic rates of H_2 and O_2 production were measured for all prepared tantalates. An outer-irradiation type fused-silica reaction cell with a volume of ∼70 mL was irradiated using a 1000 W Xe arc lamp, equipped with an IR filter, under ultraviolet ($\lambda > 230$ nm) and visible light ($\lambda > 420$ nm) radiation. The solutions were degassed by purging with N_2 for 30 min in dark conditions. Sacrificial reagents were used to show that each of the metal oxides have suitable valence and conduction band energies for water oxidation and reduction.[31]

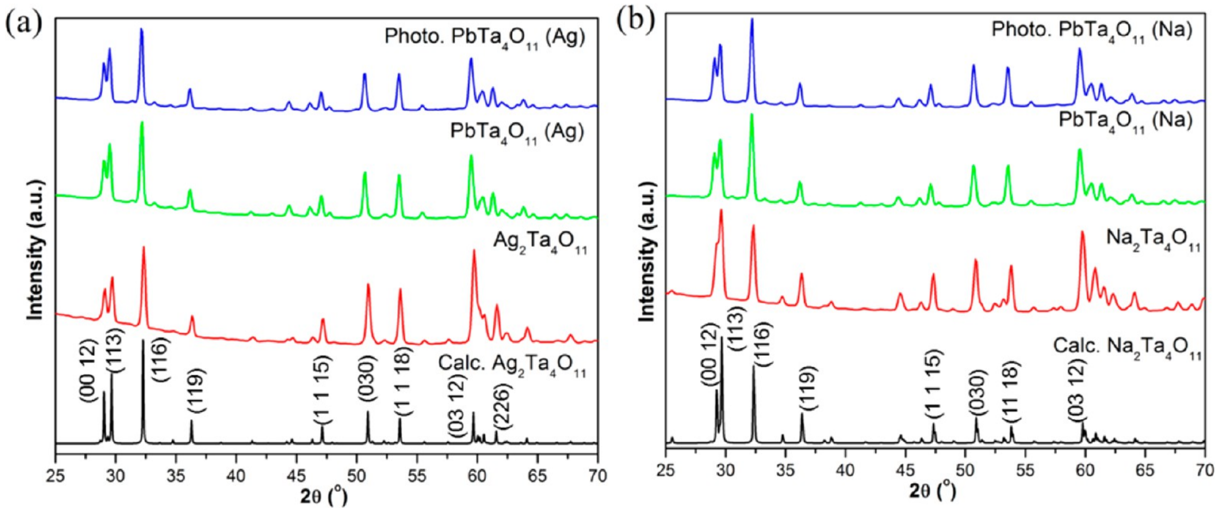

Figure 1. Calculated and experimental powder X-ray diffraction patterns of (a) $Ag_2Ta_4O_{11}$, (b) $Na_2Ta_4O_{11}$, and $PbTa_4O_{11}$ before and after photocatalytic measurements. The most intense peaks are labeled with their Miller indices (*hkl*) on the calculated patterns of $Ag_2Ta_4O_{11}$ and $Na_2Ta_4O_{11}$.

For measurements of photocatalytic H_2 production, ∼50 mg of each sample was dispersed in 20% aqueous methanol solution. Methanol acts as a hole-scavenger, photo-oxidizing to CO_2 and allowing the measurement of H_2 production without the potentially rate-limiting step of water oxidation to O_2.[32] The net balanced photocatalytic reaction under irradiation is $CH_3OH + H_2O \rightarrow 3\ H_2 + CO_2$.[7] Progress of the photocatalytic H_2 generation was recorded at 30 min intervals and used to calculate the total amount of evolved gas generated in units of μmol $H_2{\cdot}g^{-1}{\cdot}h^{-1}$.

Photocatalytic O_2 production was measured under conditions similar to those for the H_2 production measurements in a 0.050 M $AgNO_3$ solution, as has been previously reported for O_2 evolution experiments.[3] Silver nitrate serves as a sacrificial agent and is reduced to Ag(s) at the particles' surfaces.[1,3] Oxygen production rates were taken every 5 min for the first hour to record the initial rate and then every 30 min after the first hour. The amount of gas production was measured volumetrically by the displacement of a moveable liquid bubble in a horizontal quartz tube connected to the irradiated vessel. Products were identified using a gas chromatograph (SRI MG #2; helium ionization and thermal conductivity detectors) to confirm H_2, O_2, and CO_2 as the products.

Electronic Structure Calculations. Electronic structure calculations were performed on the geometry-optimized structures of $Ag_2Ta_4O_{11}$, $Pb_3Ta_4O_{13}$, $BiTa_7O_{19}$, and $Bi_7Ta_3O_{18}$ using CASTEP, a density functional theory (DFT) software package using a plane-wave basis set.[33] The Perdew−Burke−Ernzerhof functional in the generalized gradient approximation and ultrasoft core potentials were utilized in the calculations.[34]

■ RESULTS AND DISCUSSION

Synthesis and Characterization. Crystalline phases were characterized by powder X-ray diffraction techniques, and the lattice constants were refined using the JANA2006 software, as provided in the Supporting Information. The flux synthetic method with a short cooling time was utilized in the preparation of $Na_2Ta_4O_{11}$ to prevent the formation of $NaTaO_3$ impurities, as shown in Figure 1.[13] Solid-state syntheses and lead-exchange reactions of $PbCl_2$ with $A_2Ta_4O_{11}$ (*A* = Na, Ag) in air were attempted to obtain the reported $PbTa_4O_{11}$ phase,[18] but instead yielded the $Pb_3Ta_4O_{13}$ and $PbTa_2O_6$ phases, respectively. The pyrochlore $Pb_3Ta_4O_{13}$ phase crystallizes with a composition ranging from lead-deficient $Pb_{\sim 2.6}Ta_4O_{\sim 12.6}$ to lead-stoichiometric $Pb_3Ta_4O_{13}$ owing to a variable lead and oxygen content. Lead deficiency is observed in the $Pb_3Ta_4O_{13}$ phase as a peak splitting at 58° and 61° owing to randomly vacant lead sites. Vacant lead sites lead to a decrease in the lattice parameters that results in a separation of reflections that were previously coincident. However, no peak splitting was observed in the obtained products, consistent with stoichiometric $Pb_3Ta_4O_{13}$. The refined lattice constants for the products (a = 10.5427(6) Å) are consistent with the lead-stoichiometric $Pb_3Ta_4O_{13}$ (a = 10.5550(2) Å) rather than the lead-deficient $Pb_{\sim 2.6}Ta_4O_{\sim 12.6}$ phase (a = 10.4731(3) Å).[20]

The solid-state prepared $PbTa_2O_6$ phase adopts the tungsten bronze structure that exhibits metallic to semiconducting properties, depending on the lead occupancy.[21,22,35] It has previously been characterized for its dielectric properties, and its photocatalytic activity has been reported by Kato et al.[22,36] Attempts to synthesize $PbTa_2O_6$ by solid state methods with PbO and Ta_2O_5 in a 1:1 molar ratio or flux methods with $PbCl_2$ instead yielded the $Pb_3Ta_4O_{13}$ phase.[35] The lead exchange of $A_2Ta_4O_{11}$ using a 10:1 flux-to-reactant ratio in a vacuum-sealed fused-silica tube yielded the $PbTa_4O_{11}$ phase, as shown in Figure 1. As the flux-to-reactant ratio was increased from 1:1 to 10:1, the powder pattern showed shifting of the peak positions to lower 2θ, as expected, owing to the insertion of the larger Pb(II) cations between the TaO_7 pentagonal bipyramid layers of the structure. The $PbTa_4O_{11}$ products obtained using the 10:1 flux-to-reactant ratio were used for all subsequent photocatalytic, optical, and XPS measurements. The elemental compositions were confirmed by XPS measurements described below.

Structural Descriptions. The $A_2Ta_4O_{11}$ (A = Na, Ag) structures consist of layers of edge-sharing TaO_7 pentagonal bipyramids alternating with layers of TaO_6 octahedra surrounded by 7-coordinate Na(I) cations or 6-coordinate Ag(I) cations, as described previously.[12,15,18,37] The layer containing isolated TaO_6 octahedra is connected to the adjacent layers via corner sharing of the apical oxygens of the

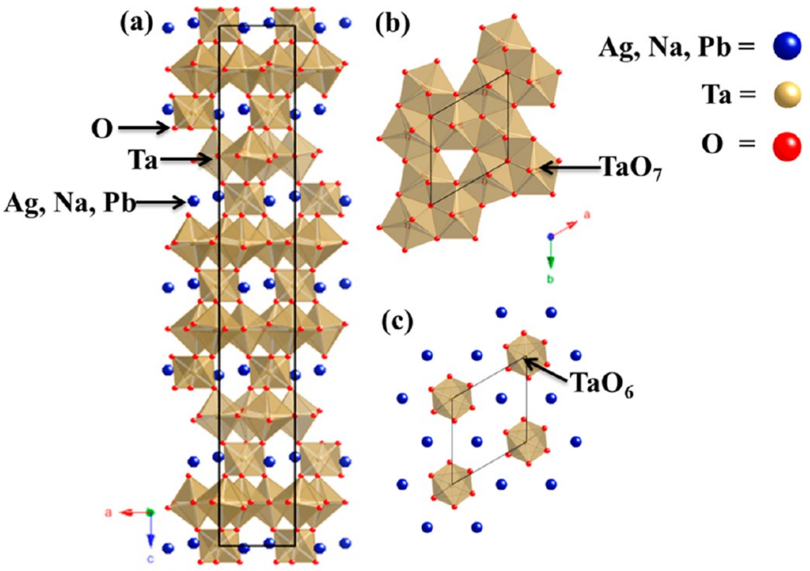

Figure 2. Polyhedral view of the unit cell of (a) $A_xTa_4O_{11}$ (A = Na, Ag, Pb; x = 1, 2) with (b) alternating layers of edge-sharing TaO_7 pentagonal bipyramids and (c) isolated TaO_6 octahedra surrounded by Na(I), Ag(I), or Pb(II) cations.

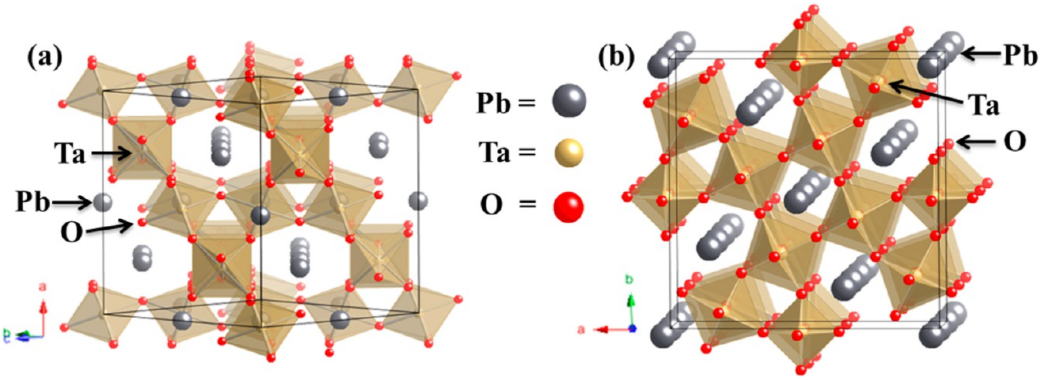

Figure 3. Polyhedral view of the unit cell for (a) $Pb_3Ta_4O_{13}$ and (b) $PbTa_2O_6$.

TaO_7 pentagonal bipyramids and are stacked down the c-axis, as shown in Figure 2. $PbTa_4O_{11}$ is structurally similar to the $A_2Ta_4O_{11}$ phases, with the Pb(II) cations surrounding the isolated TaO_6 octahedra that alternate with the TaO_7 pentagonal bipyramid layers.[18] The $Pb_3Ta_4O_{13}$ and $PbTa_2O_6$ phases differ from the $A_xTa_4O_{11}$ (A = Na, Ag, Pb; x = 1, 2) phases in that their structures consist of chains and layers of TaO_6 octahedra, respectively, as shown in Figure 3. The cubic $Pb_3Ta_4O_{13}$ structure consists of corner-sharing TaO_6 octahedra that form chains and TaO_6 six-membered rings. These TaO_6 polyhedra are further connected into complex zigzag chains throughout the structure with 8-coordinate Pb(II) cations located within the cavities. $PbTa_2O_6$ has a tungsten bronze structure that consists of 12-coordinate Pb(II) cations located within the cavities formed by layers of corner-shared TaO_6 octahedra down the c-axis.

The $BiTa_7O_{19}$ and $Bi_7Ta_3O_{18}$ structures have different local bismuth and tantalum coordination environments, as shown in Figure 4. The $BiTa_7O_{19}$ phase consists of double layers of edge-shared TaO_7 pentagonal bypyramids separated by a single layer of trigonal prismatic BiO_6 formed by the apical oxygens of the adjacent TaO_7 double layers, as previously described by Gruehn et al.[14,18] By contrast, the $Bi_7Ta_3O_{18}$ structure consists of double and single corner-shared TaO_6 octahedra chains along

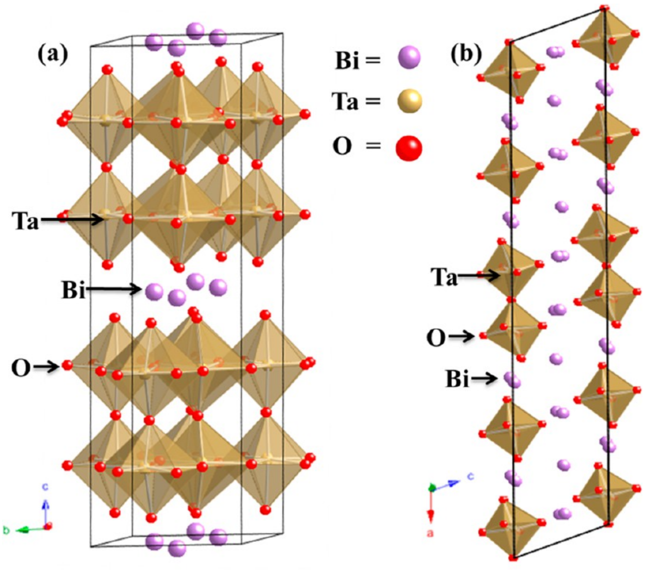

Figure 4. Polyhedral view of the unit cell for (a) $BiTa_7O_{19}$ and (b) $Bi_7Ta_3O_{18}$.

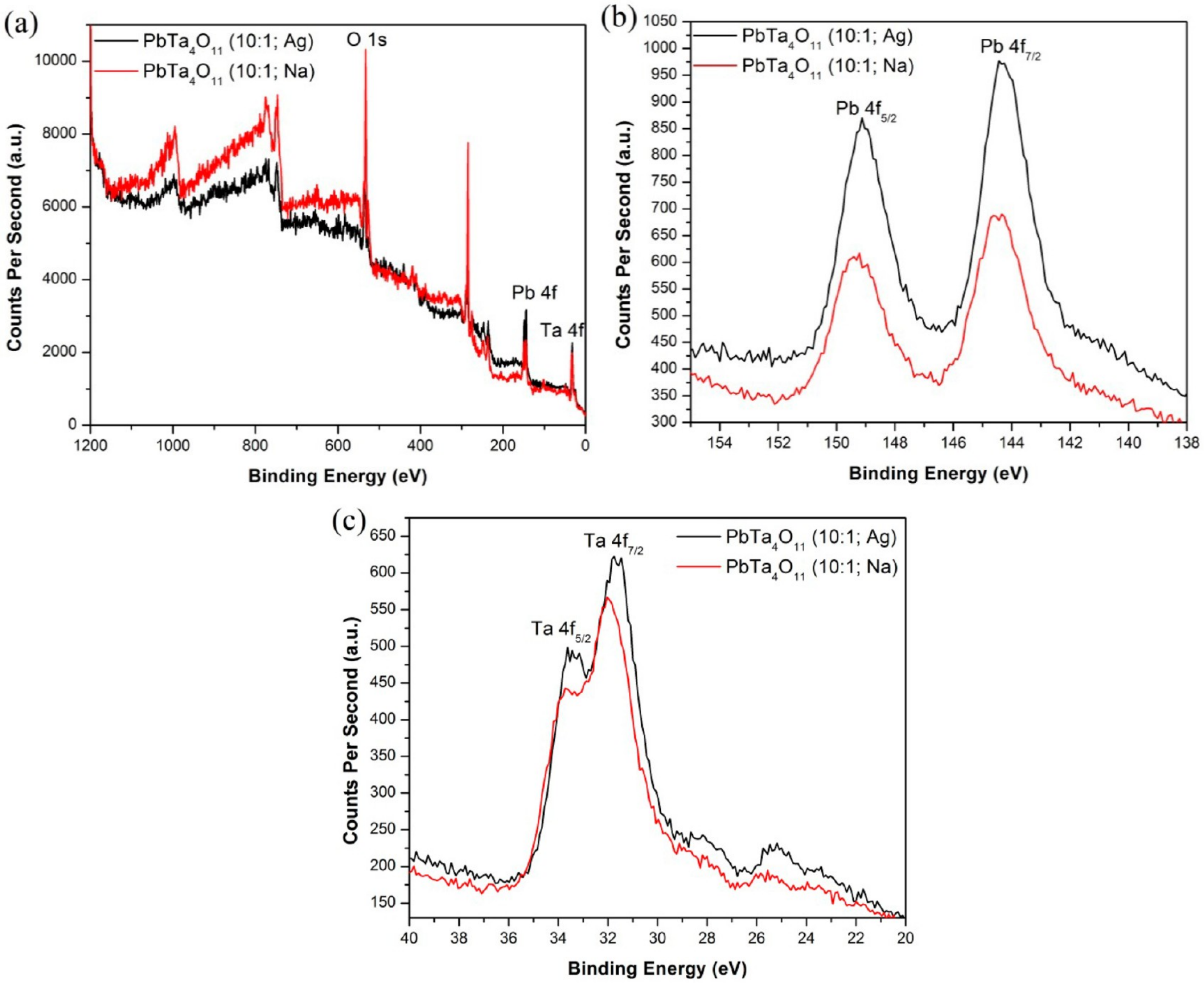

Figure 5. XPS survey scan of the (a) $PbTa_4O_{11}$ (10:1 ratio; from Ag and Na precursors) products identifying the Ta 4f, Pb 4f, and O 1s binding energy peaks and a detailed scan comparing the (b) Pb 4f and the (c) Ta 4f binding energy peak doublets for $PbTa_4O_{11}$.

the *b* axis. The chains of TaO_6 octahedra alternate with layers and chains of Bi(III) cations along the *b* and *c* directions, respectively. The coordination environments of Bi(III) cations consist distorted octahedra, distorted trigonal prisms, and square or pentagonal pyramids.[17] Thus, in $BiTa_7O_{19}$ and $Bi_7Ta_3O_{18}$, both the local and extended structure of the Bi(III) and Ta(V) cations are significantly different. However, the $BiTa_7O_{19}$ structure shares a similar layered tantalate framework described earlier for $Na_2Ta_4O_{11}$, $Ag_2Ta_4O_{11}$, and $PbTa_4O_{11}$.[13−15,17]

X-ray Photoelectron Spectroscopy (XPS). The elemental compositions of the lead-exchanged phases of $A_2Ta_4O_{11}$ (A = Na, Ag), that is, $PbTa_4O_{11}$, were probed by XPS measurements of their bulk powders. Survey scans of $PbTa_4O_{11}$ (10:1 ratio; from Ag and Na precursors) confirm the Pb 4f peak doublets, Ta 4f peak doublets, and the O 1s peak at appropriate energies, shown in Figure 5. Comparison of the detailed scans in Figure 5 of the Pb 4f binding energy peaks show the expected spin orbit splitting of ∼4.9 eV, with the two peaks corresponding to the $4f_{5/2}$ and $4f_{7/2}$ spin states at ∼149 and ∼144 eV, respectively.[27] Chemical shifts produce a second set of spin orbit split peaks shifted to lower energies at ∼148 and ∼142 eV that were deconvoluted from the overlapping peaks using the CasaXPS[25] curve-fitting software. The Pb 4f peaks were shifted by ∼6 eV to higher energies as a result of charging of the material. Variations in the surface potential caused by differential charging lead to positive space-charge buildup that shifts/distorts the binding energy peaks to higher energies.[26,38]

The Ta 4f binding energy peaks for $PbTa_4O_{11}$ are shown in Figure 5c, showing the shifted binding energy peaks as a result of the Pb(II) cations between the layers. The Ta 4f peaks of $PbTa_4O_{11}$ are shifted by ∼4 and ∼2 eV to higher binding energies relative to the Ta 4f peaks of $Ag_2Ta_4O_{11}$ and $Na_2Ta_4O_{11}$, respectively. The spin orbit splitting of the Ta $4f_{5/2}$ at higher binding energy and the Ta $4f_{7/2}$ at lower binding energy is ∼1.9 eV for $PbTa_4O_{11}$, as previously reported.[27] Peak deconvolution shows two sets of chemically shifted Ta $4f_{5/2}$ and Ta $4f_{7/2}$ peaks that are mainly a result of the alternating layers of TaO_7 and TaO_6. The higher coordination number of the tantalum in the TaO_7 pentagonal bipyramids shifts its 4f peaks to higher binding energies. The peak intensites of the TaO_7 peaks are significantly greater than that of the TaO_6 peaks owing to the 3:1 TaO_7-to-TaO_6 ratio within the layered structures. The elemental compositions calculated from the peak areas can be found in Tables S2 and S3 in the Supporting

Information. No residual Na 1s or Ag 3d peaks were detected in $PbTa_4O_{11}$. Comparison of the XPS scans from the Fermi level to 50 eV for the $A_2Ta_4O_{11}$ (A = Na, Ag) products and lead-exchanged analogues show a systematic shifting of the binding energy peaks. The materials are ordered from highest to lowest binding energies and show a decrease in binding energy with an increase in Pb(II) or Ag(I) content, as shown in Figure 6. Detailed XPS scans of the binding energy peaks for $Ag_2Ta_4O_{11}$, $Na_2Ta_4O_{11}$, and $PbTa_4O_{11}$ can be found in Figures S3−S6 in the Supporting Information.

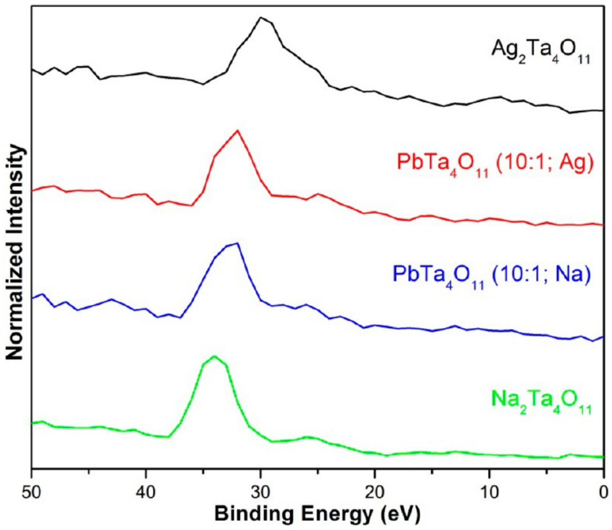

Figure 6. Comparison of the XPS scans from 0 to 50 eV binding energies for the $A_2Ta_4O_{11}$ (A = Na, Ag) products and lead-exchanged analogues ordered from highest to lowest binding energies.

Optical Properties and Electronic Structure Calculations. The optical properties and electronic structures of the metal oxides were investigated to determine their bandgap sizes, transitions, and structural relationships. The incident photon energy must be greater than the bandgap size of the metal oxide for the absorption of light and excitation of electrons.[1,3,4] UV−vis DRS measurements were taken to obtain the band gap transitions from Tauc plots of $(F(R) \times h\nu)^n$ vs $h\nu$ (eV) where $n = 2$ for direct and $n = {}^1/_2$ for indirect, as listed in Table 1 and plotted in Figure 7. Tauc plots of $Ag_2Ta_4O_{11}$ revealed an indirect bandgap size of ~3.9 eV, and a slightly larger direct transition of ~4.1 eV. This indirect bandgap size is ~0.4 eV smaller than that found for $Na_2Ta_4O_{11}$ at ~4.3 eV.[13] By comparison, $PbTa_4O_{11}$ (10:1 ratio; from Ag and Na precursors) phases exhibited indirect bandgap sizes of ~3.8−3.95 eV that slightly decreased with increasing flux-to-reactant ratios, as shown in the Supporting Information. The lead-richer cubic $Pb_3Ta_4O_{13}$ exhibited a significantly smaller indirect bandgap size of ~3.1 eV. The indirect bandgap size of the solid-state prepared $PbTa_2O_6$ was ~3.7 eV, with a slightly higher energy direct transitions at ~3.9 eV. The bismuth tantalates exhibited indirect bandgap sizes of ~3.6 eV for $BiTa_7O_{19}$ and ~2.75 eV for the bismuth-richest $Bi_7Ta_3O_{18}$ phase. The bandgap size of $Bi_7Ta_3O_{18}$ extended the deepest into the visible region of all of the investigated metal oxides. Thus, both the Pb- and Bi-richest tantalates showed the smallest bandgap sizes.

Table 1. Bandgap Sizes and Photocatalytic Rates of H_2 and O_2 Production under Ultraviolet (λ > 230 nm) Irradiation

	band gap (eV)		gas production (μmol gas·g^{-1}·h^{-1})	
composition	direct	indirect	H_2	O_2[a]
$Ag_2Ta_4O_{11}$	4.1	3.9	23	165
$Na_2Ta_4O_{11}$	4.5	4.3	34	110
$PbTa_4O_{11}$ (Ag)[b]	4.1	3.8	175	181
$PbTa_4O_{11}$ (Na)[c]	4.15	3.95	72	107
$Pb_3Ta_4O_{13}$	3.4	3.0	7	42
$PbTa_2O_6$	3.9	3.6	23	213
$BiTa_7O_{19}$	3.75	3.6	194	140
$Bi_7Ta_3O_{18}$	3.10	2.75	31	113

[a] The rate of O_2 evolution was calculated on the basis of the first 1 h because the concurrent photodeposition of Ag(s) at the surfaces decreased the rate over time. [b,c] Photocatalytic rates and band gaps of $PbTa_4O_{11}$ (from Ag and Na precursors) prepared from 10:1 flux-to-reactant products.

To investigate the structural origins of the bandgap sizes and the nature of the bandgap transitions, electronic structure calculations were performed for $Ag_2Ta_4O_{11}$, $Pb_3Ta_4O_{13}$, $BiTa_7O_{19}$, and $Bi_7Ta_3O_{18}$ with the use of DFT methods in the software package CASTEP. Previous calculations on $Na_2Ta_4O_{11}$ confirmed that its lowest-energy indirect band gap transition arises between filled O 2p crystal orbitals and the empty Ta 5d crystal orbitals, with contributions from both the TaO_7 pentagonal bipyramid layers and the isolated TaO_6 octahedra.[13] The electronic band structures confirm the nature of the lowest energy band gap transition as indirect for each metal oxide, as shown in Figures 8 and 9 and in the Supporting Information. The band structures for $Ag_2Ta_4O_{11}$, $Pb_3Ta_4O_{13}$, and $Bi_7Ta_3O_{18}$ structures confirmed slightly higher energy direct transitions at the Γ-points. For example, in $Pb_3Ta_4O_{13}$, the indirect band gap occurs from the R-point to the Γ-point, shown in Figure 8. In $BiTa_7O_{19}$, Figure 9, the lowest energy direct transition lies at the H-point, and the indirect transition occurs from the K-point to the H-point.

Partial Densities-Of-States (PDOS) and electron density plots for each structure are shown in Figures 10 and 11 and in the Supporting Information. The atomic contributions to the lowest conduction and highest valence-band states are illustrated in these plots. The highest-energy valence-band states of $Ag_2Ta_4O_{11}$, $Pb_3Ta_4O_{13}$, $BiTa_7O_{19}$, and $Bi_7Ta_3O_{18}$ consist of filled Ag 4d orbitals, Pb 6s orbitals, and Bi 6s orbitals, respectively, mixed with O 2p orbitals. Their lowest-energy conduction-band states all primarily consist of empty Ta 5d orbitals. Interaction of the O 2p orbitals with the filled $4d^{10}$ orbitals of Ag(I), $6s^2$ orbitals of Pb(II), and $6s^2$ orbitals of Bi(III) result in positively shifted valence band states and a reduction in their bandgap sizes. The valence band energies consisting primarily of O 2p orbital contributions for $Na_2Ta_4O_{11}$ are positively shifted when mixed with Ag 4d and Pb 6s orbital contributions for $Ag_2Ta_4O_{11}$ and $PbTa_4O_{11}$, respectively. A positive shift in the valence band energies is, as found in the XPS data, from the decrease in the binding energy with an increase in the Ag(I) or Pb(II) content, as shown in Figure 6.

A larger dispersion of the bands results in a smaller bandgap size and effective mass. Electrons with smaller effective masses have higher mobilities, such as found within the layered structure of $BiTa_7O_{19}$.[39] The cubic $Pb_3Ta_4O_{13}$ structure contains zigzag TaO_6 chains surrounded by Pb(II) cations, whereas the $Bi_7Ta_3O_{18}$ structure contains single and double

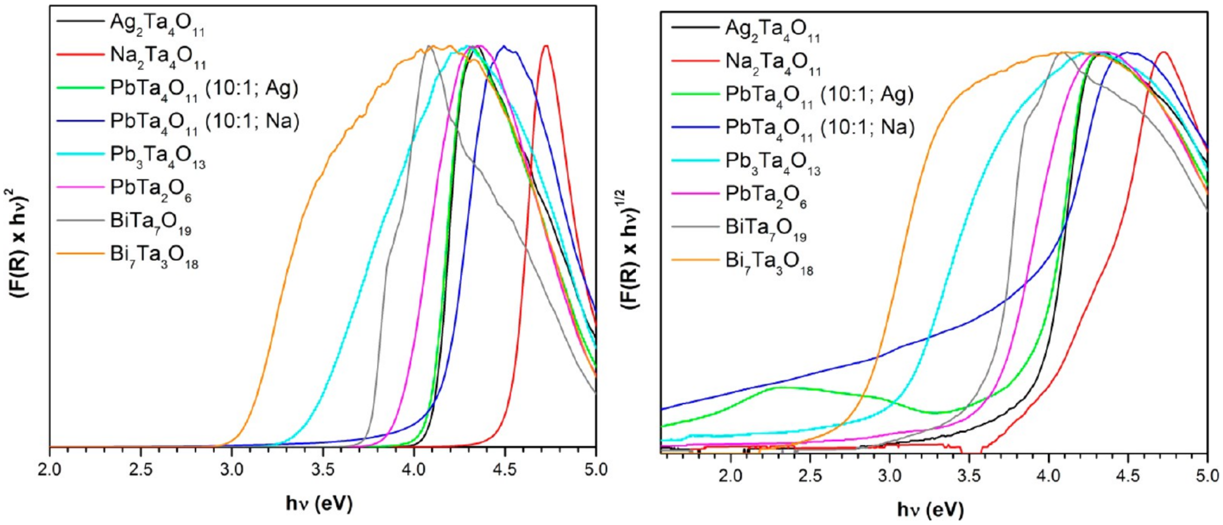

Figure 7. UV−vis diffuse reflectance spectra were plotted as Tauc plots of $(F(R) \times h\nu)^n$ vs $h\nu$ (eV) for direct ($n = 2$) and indirect ($n = {}^1/_2$) band gap transitions of all phases.

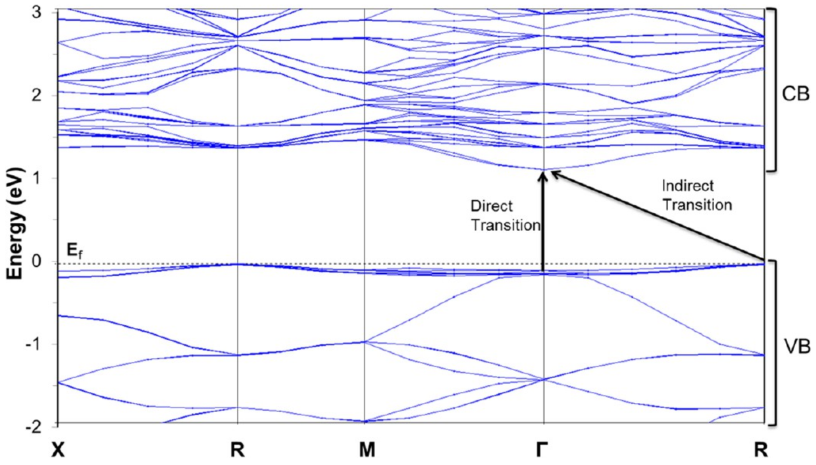

Figure 8. The band structure for $Pb_3Ta_4O_{13}$ with the direct band gap transition shown at the Γ point and the indirect band gap transition from the R point to the Γ point in reciprocal space.

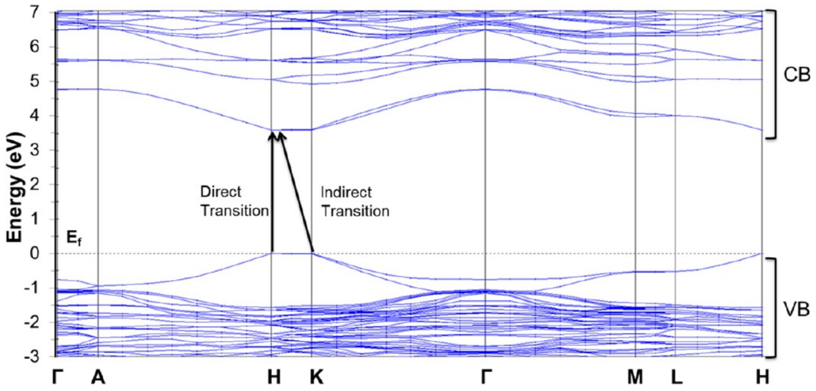

Figure 9. The band structure for $BiTa_7O_{19}$ with the lowest-energy direct bandgap transition shown at the H-point and the indirect bandgap transition from the K-point to the H-point in reciprocal space.

one-dimensional TaO_6 chains surrounded by Bi(III) ions. Lower charge carrier mobility in the conduction band of $Pb_3Ta_4O_{13}$ and $Bi_7Ta_3O_{18}$ would be expected according to the electronic band structure calculations, which show that the conduction bands exhibit a lower degree of band dispersion. Electron density plots show the conduction band states primarily consist of Ta 5d orbitals that are delocalized over the TaO_7 pentagonal bipyramid layers in $Ag_2Ta_4O_{11}$ and $BiTa_7O_{19}$ as well as the TaO_6 octahedra in $Ag_2Ta_4O_{11}$. The $Pb_3Ta_4O_{13}$ and $Bi_7Ta_3O_{18}$ phases show electron density in their lowest-energy conduction-band states delocalized across chains of corner-sharing TaO_6 octahedra. Excited electrons are thus

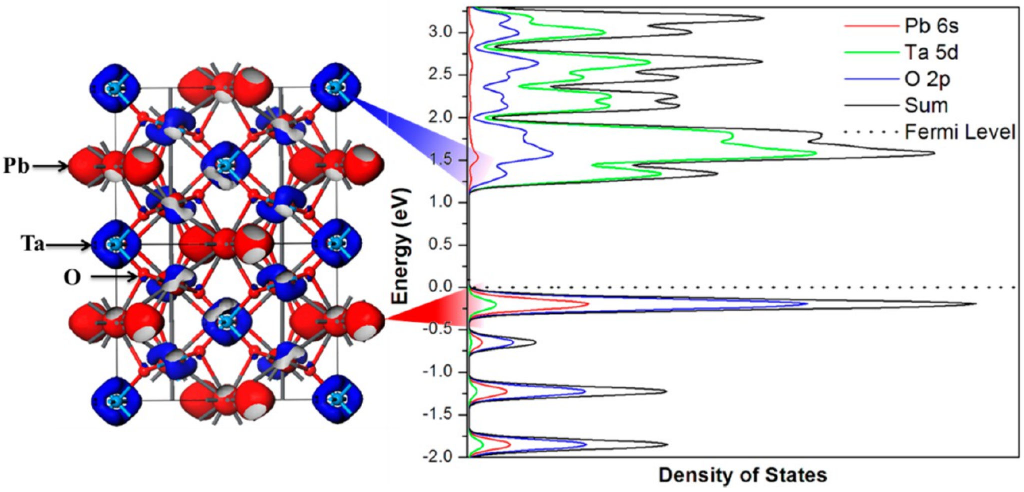

Figure 10. The densities-of-states (DOS; right) and electron density plots (left) of $Pb_3Ta_4O_{13}$. The individual atomic contributions are projected out in the DOS, and the electron density at the top of the valence band and bottom of the conduction band are shaded red and blue, respectively.

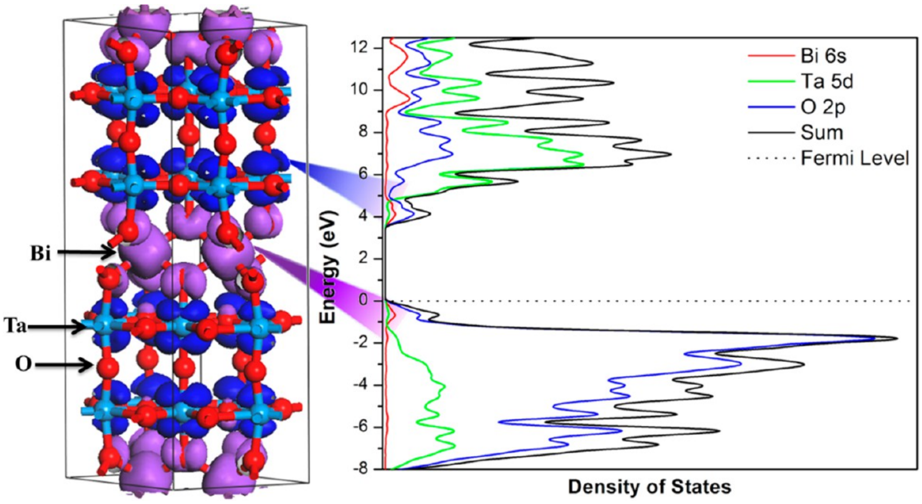

Figure 11. The densities-of-states (DOS; right) and electron density plots (left) of $BiTa_7O_{19}$. The individual atomic contributions are projected out in the DOS, and the electron density at the top of the valence band and bottom of the conduction band are shaded purple and blue, respectively.

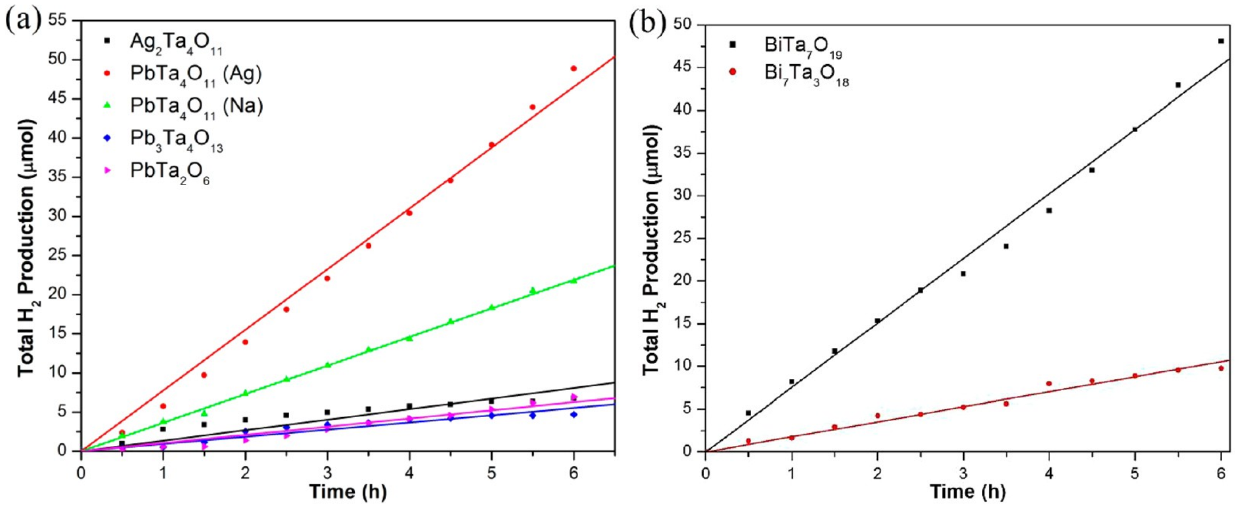

Figure 12. Photocatalytic hydrogen production (μmol H_2) versus time (h) for $Ag_2Ta_4O_{11}$, $Na_2Ta_4O_{11}$, $PbTa_4O_{11}$ (10:1; Ag and Na precursors), $Pb_3Ta_4O_{13}$, and $PbTa_2O_6$ (a) and the two bismuth tantalates $BiTa_7O_{19}$ and $Bi_7Ta_3O_{18}$ (b) under ultraviolet and visible-light ($\lambda > 230$ nm) irradiation.

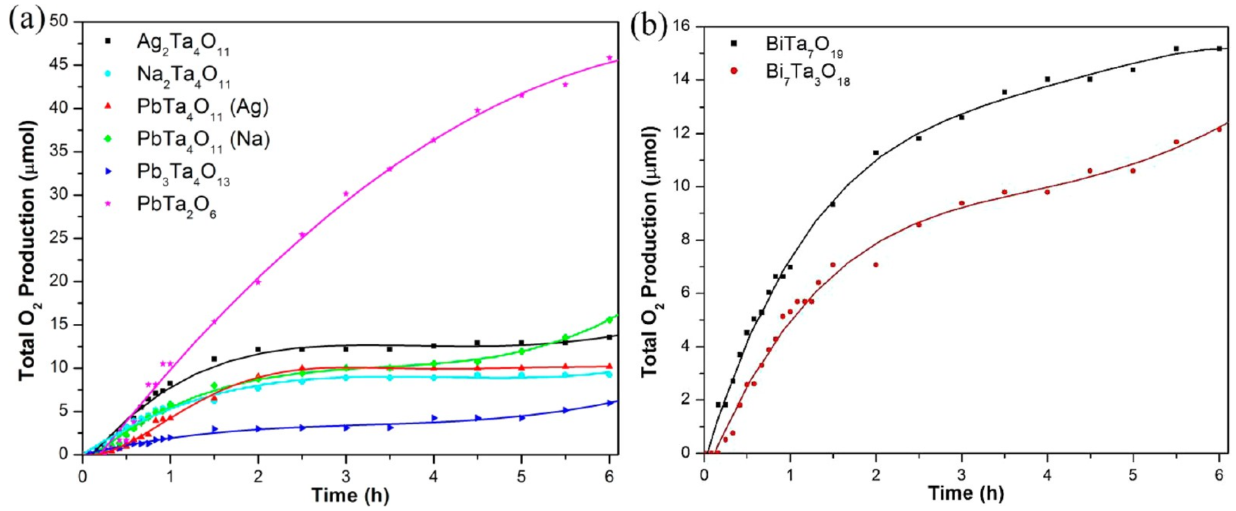

Figure 13. Photocatalytic oxygen production (μmol O_2) versus time (h) for $Ag_2Ta_4O_{11}$, $Na_2Ta_4O_{11}$, $PbTa_4O_{11}$ (10:1 ratio; from Ag and Na precursors), $Pb_3Ta_4O_{13}$, and $PbTa_2O_6$ (a) and the two bismuth tantalates $BiTa_7O_{19}$ and $Bi_7Ta_3O_{18}$ (b) under ultraviolet and visible-light ($\lambda > 230$ nm) irradiation.

predicted to be delocalized along these tantalate layers and chains. This has been previously observed for the layered perovskite $ALaNb_2O_7$ (A = Rb, Ag) consisting of a double layer of corner-sharing NbO_6 octahedra.[7] A larger band dispersion of the lowest-energy conduction bands in directions along the two-dimensional layers is indicative of higher charge-carrier mobility within the niobate layers. By contrast, flat bands with little band dispersion are indicative of lower charge carrier mobility perpendicular to the niobate layers, that is, along the *c*-axis direction.[7]

Photocatalytic Properties. The metal oxides were investigated for their photocatalytic activity for H_2 and O_2 production from aqueous solution, as shown in Figures 12 and 13 and listed in Table 1. After photocatalytic measurements, all metal oxides were again characterized by PXRD to confirm their stability under the testing conditions. No photodegradation was observed in any of the samples after UV irradiation in the aqueous solutions. No photocatalytic H_2 or O_2 production from aqueous solutions was observed under visible-light irradiation ($\lambda > 420$ nm). Previously reported photocatalytic activities of the related $Na_2Ta_4O_{11}$ ranged from ~13.4 to ~34.1 μmol $H_2 \cdot g^{-1} \cdot h^{-1}$, depending on the flux preparation conditions.[13]

The metal oxide with the highest rate of H_2 production was $PbTa_4O_{11}$, with a rate of ~175 μmol $H_2 \cdot g^{-1} \cdot h^{-1}$, whereas the precursor $Ag_2Ta_4O_{11}$ had a rate of only ~23 μmol $H_2 \cdot g^{-1} \cdot h^{-1}$. In comparison, the $PbTa_4O_{11}$ prepared from the lead-exchange reaction of $Na_2Ta_4O_{11}$ yielded a ~50% lower photocatalytic rate of ~72 μmol $H_2 \cdot g^{-1} \cdot h^{-1}$. XPS scans show there is a higher amount of Pb(II) at the surfaces in the former $PbTa_4O_{11}$ preparation (Supporting Information Tables S2 and S3), likely leading to its higher activity. The other Pb(II)-containing phases, $PbTa_2O_6$ and $Pb_3Ta_4O_{13}$, exhibited even lower photocatalytic rates of ~23 μmol $H_2 \cdot g^{-1} \cdot h^{-1}$ and ~7 μmol $H_2 \cdot g^{-1} \cdot h^{-1}$, respectively. These two Pb(II)-based tantalates had the smaller bandgap sizes and thus could absorb a broader energetic range of photons; however, their structures consist of condensed TaO_6 octahedra, rather than layers of TaO_7 pentagonal bipyramids as found in $PbTa_4O_{11}$.

A similar trend was observed for the bismuth tantalates. The yellow $BiTa_7O_{19}$ and $Bi_7Ta_3O_{18}$ photocatalysts had rates of ~194 and ~31 μmol $H_2 \cdot g^{-1} \cdot h^{-1}$, respectively. Although $Bi_7Ta_3O_{18}$ had the smaller band gap (~2.75 eV vs ~3.6 eV) of the two, it exhibited a much lower H_2 production rate than that of $BiTa_7O_{19}$. Thus, structural features present in $Pb_3Ta_4O_{13}$ and $Bi_7Ta_3O_{18}$ are not as favorable for the charge separation and migration of the excited electrons to the surface as compared with the delocalized two-dimensional TaO_7 layers. Electronic structure calculations show the delocalization of excited electrons across the TaO_7 pentagonal bipyramid layers within the $A_2Ta_4O_{11}$ (A = Na, Ag), $PbTa_4O_{11}$, and $BiTa_7O_{19}$ structures. Significant photocatalytic H_2 production for materials containing MO_6 (M = Ti, Nb, Ta) layered structural features have previously been extensively investigated.[1,3,7]

The photocatalytic rates for O_2 production were calculated from the initial rates, as shown in Figure 13. The O_2 rates decrease over time as Ag(s) deposits on the particles' surface owing to its reduction as a sacrificial reagent. These silver deposits coat the particles' surface and inhibit further O_2 generation, as confirmed by Domen et al.[40−43] The photocatalyst with the highest O_2 production rate was $PbTa_2O_6$ at ~213 μmol $O_2 \cdot g^{-1} \cdot h^{-1}$, compared with the pyrochlore $Pb_3Ta_4O_{13}$ that produced ~42 μmol $O_2 \cdot g^{-1} \cdot h^{-1}$. The $PbTa_4O_{11}$ phase generated ~181 μmol $O_2 \cdot g^{-1} \cdot h^{-1}$, whereas its precursor $Ag_2Ta_4O_{11}$ exhibited a similar rate of ~165 μmol $O_2 \cdot g^{-1} \cdot h^{-1}$. The production rates for $Na_2Ta_4O_{11}$ and its lead-exchanged phase $PbTa_4O_{11}$ were ~107 and ~110 μmol $O_2 \cdot g^{-1} \cdot h^{-1}$, respectively. Thus, the lead exchange of $Na_2Ta_4O_{11}$ or $Ag_2Ta_4O_{11}$, in the preparation of $PbTa_4O_{11}$, had almost no measurable effect on their photocatalytic activity for O_2 production. This is surprising, given the role of the valence band states, that is, the Pb 6s or O 2p orbitals, in water oxidation. $BiTa_7O_{19}$ had a rate of ~140 μmol $O_2 \cdot g^{-1} \cdot h^{-1}$, and the $Bi_7Ta_3O_{18}$ phase generated ~113 μmol $O_2 \cdot g^{-1} \cdot h^{-1}$. Only $BiTa_7O_{19}$ exhibited a higher rate of H_2 versus O_2 production; all other metal oxides showed a significantly higher O_2 production rates. Thus, nearly all of these metal oxides more efficiently as water oxidation catalysts.

Photocatalytic gas generation was observed in the absence of the sacrificial reagents for individual photocatalytic H_2 and O_2 production. The platinized $PbTa_4O_{11}$ (10:1 ratio; from Ag precursors) and $BiTa_7O_{19}$ phases exhibited water splitting in deionized water under UV irradiation. The Pb(II)- and Bi(III)-based tantalates containing TaO_7 pentagonal bipyramid layers produced ∼17 and ∼34 μmol $g^{-1}\cdot h^{-1}$, respectively. Gas chromatography using a thermal conductivity detector confirmed both H_2 and O_2 were generated during the reactions, with a significant portion of O_2 as the product. The pH of the solution after photocatalytic measurements decreased from ∼7 to ∼3.75−3.85 owing to the accumulation of protons in solution. Thus, these metal oxides functioned more efficiently as water oxidation catalysts.

CONCLUSIONS

The Ag(I)-, Pb(II)-, and Bi(III)-based tantalates $Ag_2Ta_4O_{11}$, $PbTa_2O_6$, $BiTa_7O_{19}$, and $Bi_7Ta_3O_{18}$ can be prepared by solid state methods at 1000−1100 °C for 24−48 h. The Pb(II)-containing tantalates $Pb_3Ta_4O_{13}$ and $PbTa_4O_{11}$ (10:1 ratio; from Ag and Na precursors) can be prepared with a $PbCl_2$ flux at 700 °C from 24 to 96 h. UV−vis diffuse reflectance measurements were used to obtain the lowest-energy indirect band gaps of $Ag_2Ta_4O_{11}$ (∼3.9 eV), $PbTa_4O_{11}$ (∼3.8−3.95 eV), $Pb_3Ta_4O_{13}$ (∼3.0 eV), $PbTa_2O_6$ (∼3.6 eV), $BiTa_7O_{19}$ (∼3.6 eV), and $Bi_7Ta_3O_{18}$ (∼2.75 eV). A decrease in the band gap was observed with an increase in the Pb(II) or Bi(III) content. Photocatalytic rates of the platinized samples under ultraviolet and visible light ranged from ∼7 to ∼194 μmol $H_2\cdot g^{-1}\cdot h^{-1}$ in aqueous methanol and from ∼42 to ∼213 μmol $O_2\cdot g^{-1}\cdot h^{-1}$ in aqueous silver nitrate. Only $PbTa_4O_{11}$ and $BiTa_7O_{19}$ exhibited overall water-splitting photocatalysis in deionized water, with rates of ∼17 and ∼34 $\mu mol\cdot g^{-1}\cdot h^{-1}$, respectively. Electronic-structure calculations show the highest-energy valence band states consist of the respective Ag 4d orbital/Pb 6s orbital/Bi 6s orbital and O 2p orbital contributions, and the lowest-energy conduction band states arise from the Ta 5d orbital contributions. The latter are delocalized over the TaO_7 pentagonal bipyramid layers within the $A_2Ta_4O_{11}$ (A = Na, Ag), $PbTa_4O_{11}$, and $BiTa_7O_{19}$ structures. Higher activity for water reduction was found for tantalates consisting of TaO_7 pentagonal bipyramid layers that can serve as extended charge-migration pathways.

ASSOCIATED CONTENT

Supporting Information

Powder X-ray diffraction patterns of $Pb_3Ta_4O_{13}$, $PbTa_2O_6$, $BiTa_7O_{19}$, and $Bi_7Ta_3O_{18}$ products before and after photocatalysis measurements; refined lattice parameters for all products; quantitative analysis of compositions from XPS data; detailed XPS scans of $Ag_2Ta_4O_{11}$ and lead-exchanged products; UV−vis DRS of lead-exchanged products with varied flux-to-reactant ratios; electronic band structures; partial density of states; and initial oxygen production rate graphs. This information is available free of charge via the Internet at http://pubs.acs.org/

AUTHOR INFORMATION

Corresponding Author

*E-mail: pamaggar@ncsu.edu.

Notes

The authors declare no competing financial interest.

ACKNOWLEDGMENTS

Support of this research from the Research Corporation for Science Advancement (P.M. is a Scialog Awardee) is acknowledged. The authors would like to acknowledge Dr. Daniel Dougherty and Sean Stuart for their assistance in data collection on their XPS instrument to investigate $A_xTa_4O_{11}$ (A = Na(I), Ag(I), Pb(II); x = 1, 2) phases.

REFERENCES

(1) Kudo, A.; Miseki, Y. *Chem. Soc. Rev.* **2009**, *38*, 253−78.
(2) Kitano, M.; Hara, M. *J. Mater. Chem.* **2010**, *20*, 627.
(3) Osterloh, F. E. *Chem. Mater.* **2008**, *20*, 35−54.
(4) Lewis, N. S. *Nature* **2001**, *414*, 589−90.
(5) Kato, H.; Asakura, K.; Kudo, A. *J. Am. Chem. Soc.* **2003**, *125*, 3082−9.
(6) Huang, L.; Peng, F.; Yu, H.; Wang, H. *Solid State Sci.* **2009**, *11*, 129−138.
(7) Arney, D.; Maggard, P. A. *ACS Catal.* **2012**, *2*, 1711−1717.
(8) Domen, K.; Yoshimura, J.; Sekine, T. *Catal. Lett.* **1990**, *4*, 1−5.
(9) Kim, H. G.; Becker, O. S.; Jang, J. S.; Ji, S. M.; Borse, P. H.; Lee, J. S. *J. Solid State Chem.* **2006**, *179*, 1214−1218.
(10) Porob, D. G.; Maggard, P. A. *J. Solid State Chem.* **2006**, *179*, 1727−1732.
(11) Domen, K.; Hara, M.; Kondo, J. *Korean J. Chem. Eng.* **2001**, *18*, 862−866.
(12) Mattes, R.; Schaper, J. *Rev. Chim. Miner.* **1985**, *22*, 817−820.
(13) Mclamb, N.; Sahoo, P. P.; Fuoco, L.; Maggard, P. A. *Cryst. Growth Des.* **2013**, *13*, 2322−2326.
(14) Darstellung, Z.; Gruehn, R. *Z. Anorg. Allg. Chem.* **1990**, *581*, 183−189.
(15) Masó, N.; Woodward, D. I.; Thomas, P. A.; Várez, A.; West, A. R. *J. Mater. Chem.* **2011**, *21*, 2715−2722.
(16) Zhou, W. *Adv. Mater.* **1990**, *2*, 414−418.
(17) Ling, C. D.; Schmid, S.; Withers, R. L.; Thompson, J. G.; Ishizawa, N.; Kishimoto, S. *Acta Crystallogr.* **1999**, *55*, 157−164.
(18) Stemmer, W.; Gruehn, R. *Z. Anorg. Allg. Chem.* **1993**, *619*, 409−415.
(19) Beech, F.; Michaela, W.; Catlow, C. R. A.; Kingdom, U.; Steele, B. C. H. *J. Solid State Chem.* **1988**, *77*, 322−335.
(20) Scott, H. G. *J. Solid State Chem.* **1982**, *139*, 131−139.
(21) Francombe, M. H. *Acta Crystallogr.* **1958**, *11*, 696−703.
(22) Hornebecq, V.; Elissalde, C.; Gravereau, P.; Lebraud, E.; Ravez, J. *J. Solid State Chem.* **2001**, *157*, 261−273.
(23) Simmons, E. L. *Appl. Opt.* **1976**, *15*, 951−4.
(24) Morales, A. E.; Mora, E. S.; Pal, U. *Rev. Mex. Fis.* **2007**, *53*, 18−22.
(25) Fairley, N. *CasaXPS*; 2011.
(26) Hofmann, S. *Auger- and X-Ray Photoelectron Spectroscopy in Materials Science*; Springer: New York, 2012.
(27) Moulder, J. F.; Stickle, W. F.; Sobol, P. E.; Bomben, K. D. *Handbook of X-ray Photoelectron Spectroscopy*; Chastain, J., King, R. C., J., Eds.; Physical Electronics, Inc.: Eden Prairie, MN, 1992.
(28) Yang, J.; Wang, D.; Han, H.; Li, C. *Acc. Chem. Res.* **2013**, *46*, 1900−1909.
(29) Ohtani, B.; Iwai, K.; Nishimoto, S.; Sato, S. *J. Phys. Chem. B* **1997**, *5647*, 3349−3359.
(30) Nakamatsu, H.; Kawai, T. *J. Chem. Soc., Faraday Trans.* **1986**, *82*, 527−531.
(31) Liu, H.; Yuan, J.; Shangguan, W. *Energy Fuels* **2006**, *20*, 2289−2292.
(32) Graetzel, M. E. *Energy Resources through Photochemistry and Catalysis*; Academic Press: New York, 1983.
(33) Clark, S. J.; Segall, M. D.; Pickard, C. J.; Hasnip, P. J.; Probert, M. I. J.; Refson, K.; Payne, M. C. *Z. Kristallogr.* **2005**, *220*, 567−570.
(34) Payne, M. C.; Arias, T. A.; Joannopoulos, J. D. *Rev. Mod. Phys* **1992**, *64*, 1045−1097.
(35) Subbarao, E. C.; Shirane, G.; Jona, F. *Acta Crystallogr.* **1960**, *13*, 226−231.
(36) Kato, H.; Kudo, A. *Chem. Phys. Lett.* **1998**, *295*, 487−492.
(37) Ercit, T. S.; Hawthorne, F. C.; Cerny, P. *Bull. Miner.* **1985**, *108*, 541−549.

(38) Van Der Heide, P. *X-ray Photoelectron Spectroscopy: An Introduction to Principles and Practices*; Wiley: Hoboken, NJ, 2012.
(39) Woodward, P. M.; Mizoguchi, H.; Kim, Y. I.; Stoltzfus, M. W. In *Metal Oxides: Chemistry and Applications*; Fierro, J. L. G., Ed.; CRC Press: Hoboken, NJ, 1988; pp 158−160.
(40) Ogisu, K.; Ishikawa, A.; Teramura, K.; Toda, K.; Hara, M.; Domen, K. *Chem. Lett.* **2007**, *36*, 854−855.
(41) Ishikawa, A.; Takata, T.; Kondo, J. N.; Hara, M.; Kobayashi, H.; Domen, K. *J. Am. Chem. Soc.* **2002**, *124*, 13547−53.
(42) Maeda, K.; Wang, X.; Nishihara, Y.; Lu, D.; Antonietti, M.; Domen, K. *J. Phys. Chem. C* **2009**, *113*, 4940−4947.
(43) Nukumizu, K.; Nunoshige, J.; Takata, T.; Kondo, J. N.; Hara, M. *Chem. Lett.* **2003**, *32*, 196−197.